RESEARCH ARTICLE

Electrochemical growth of α-MnO$_2$ on carbon fibers for high-performance binder-free electrodes of supercapacitors

Ya Chen[1] · Jie-Hao Guan[1] · Hui Gan[1] · Bai-Zhen Chen[1] · Xi-Chang Shi[1]

Abstract

Cryptomelane-type MnO$_2$ (α-MnO$_2$) was directly deposited on carbon fiber paper (CFP) by a simple electrochemical method and evaluated as the active material of binder-free electrodes for supercapacitors. The obtained α-MnO$_2$@CFP electrode exhibits a higher capacitance and better rate capability than the ε-MnO$_2$@CFP electrode prepared by the conventional electrochemical method. For the α-MnO$_2$@CFP electrode, a specific capacitance of 623.9 F g^{-1} can be achieved at 2 mV s^{-1} and the capacitance retention is up to 75% at 200 mV s^{-1}. Compared to most of the binder-free MnO$_2$/carbon electrodes reported in previous studies, the electrode also presents a much better rate capability. These superiorities mainly result from the specific tunnel structure of α-MnO$_2$ which offers not only facile diffusion paths for cations but also plentiful reactive sites for the inner-surface redox reactions associated with the energy storage process. The fabrication method is facile and readily scalable and thus has great promise in the development of high-performance binder-free MnO$_2$ electrodes for energy storage devices.

Graphical Abstract
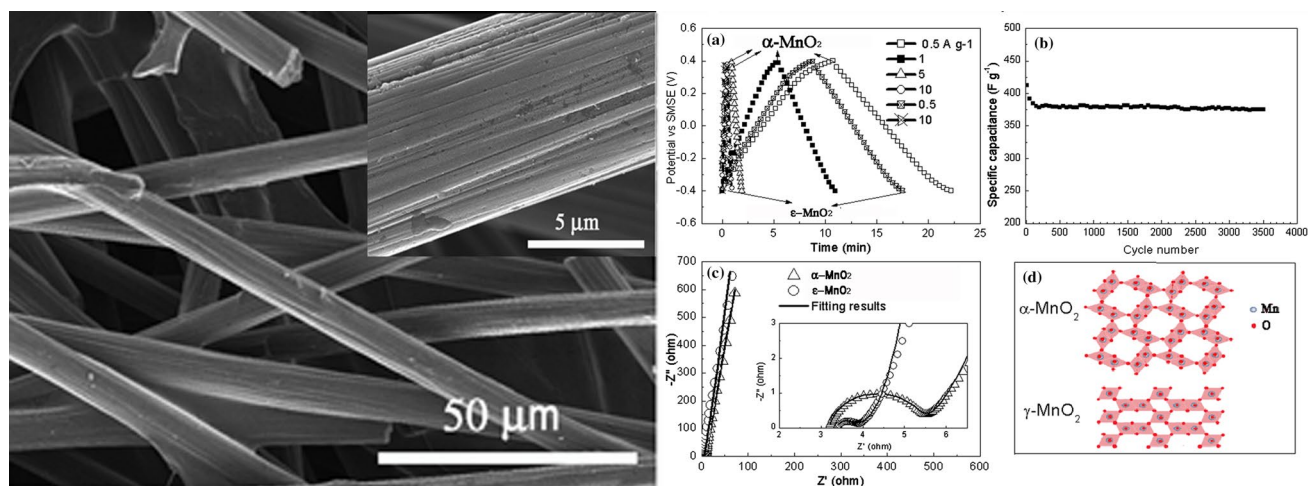
Keywords Supercapacitor · Binder-free electrode · Manganese dioxide · Cryptomelane structure · Rate capability

✉ Ya Chen
chenya1973a@sina.com

1   School of Metallurgy and Environment, Central South University, Changsha 410083, China

1 Introduction

MnO$_2$ has been investigated as one of the most attractive electrode materials for supercapacitors due to its high theoretical capacitance, low cost, environmental friendliness, and natural abundance [1–5]. To improve the electronic

conductivity of this material, considerable efforts have been devoted to the development of various MnO_2 composites among which MnO_2/carbon composites attract much attention. To date, different carbonaceous materials, such as graphene [6–9], carbon nanotubes (CNTs) [10–12], activated carbon [13, 14], and mesoporous carbon [15–18], have been used to prepare these composites. It is believed that the carbon materials in these MnO_2 composites can provide good conductive paths and thus help to effectively utilize the redox property of MnO_2. Considering the fact that powdery carbon/MnO_2 materials need to be mixed with polymeric adhesives to form electrodes, and this possibly introduces unnecessary charge-transfer barriers among the active materials, a great deal of attention has been focused on the development of binder-free carbon/MnO_2 electrodes [19–21].

In most cases, carbon materials with different nanostructures were constructed and used as the backbones on which MnO_2 was directly electrodeposited from neutral $MnSO_4$ solutions. As a result, the MnO_2 of the obtained binder-free electrodes usually exhibits a ramsdellite-type (R or γ-type) or akhtenskite-type (ε-type) structure with 2×1 [MnO_6] tunnels [21, 22]. Although high specific capacitances can be achieved, the capacitance retention of these binder-free electrodes is relatively low and further improvement is still necessary.

It is known that MnO_2 exists in several crystallographic forms including α, β, and γ, among which the α-MnO_2 seems to exhibit a much higher capacitance than others [23, 24]. However, most of the studies were carried out on powdery electrodes in which polymeric adhesive and conductive additives had to be added. The distribution of the additives and the process of electrode fabrication may have a significant influence on the performance of the obtained electrodes and thus lead to uncertainty in the performance comparison. Furthermore, to the best of our knowledge, although α-MnO_2 is easily prepared by hydrothermal methods, electrochemical growth of α-MnO_2 on carbon substrates or other current collectors has seldom been reported [25]. In the present work, cryptomelane-type MnO_2 (α-MnO_2) was directly electrodeposited on carbon fiber paper (CPF) by a simple method and evaluated as the active material of binder-free electrodes for supercapacitors. Comparisons of the electrochemical properties between the α-MnO_2 and ε-MnO_2 are also presented.

2 Experimental section

All the reagents were analytical grade and used directly without further purification. Rectangular carbon fiber paper (CPF) slabs (1×2 cm^2) were ultrasonically cleaned in acetone, deionized water, and ethanol sequentially for 15 min each, then dried and used as the carbon substrates. The electrochemical

deposition of α-MnO_2 was carried out in an aqueous solution containing 2 M H_2SO_4 and 0.5 M $MnSO_4$ at 15 °C. The deposition process was monitored at a constant current density of 8 mA cm^{-2} using a CHI660B electrochemical workstation (Shanghai Chenhua Instrument Co.). A CFP slab with a working area of 1 cm^2 and a titanium plate with a working area of 9 cm^2 were used as the working and counter electrodes, respectively. After deposition, the obtained MnO_2@CFP slab was washed with deionized water and dried. For comparison, a common ε-MnO_2 coating was also deposited on a CFP slab from a solution containing 0.5 M Na_2SO_4 and 0.5 M $MnSO_4$ with the same procedure but at room temperature (about 25 °C).

The surface morphology and microstructure of the oxide were examined with a scanning electron microscope (JEOL JSM-6060LA) and a field-emission transmission electron microscope (TEM, Hitachi HT7700 operated at 120 kV), respectively. X-ray diffraction (XRD) analyses were performed using a Rigaku-TTRIII with graphite-monochromatized high-intensity Cu Kα radiation. The oxidation states of manganese in the oxide were determined by X-ray photoelectron spectroscopy (XPS), which were carried out using a source (PE = 1600 eV) on a Kratos Axis Ultra DLD instrument with monochromatic Al K.

The electrochemical properties of the MnO_2 were evaluated using a three-electrode electrochemical cell in conjunction with the CHI660B electrochemical workstation at room temperature. The MnO_2@CFP slab, a platinum sheet, and a saturated mercury/mercurous sulfate electrode (SMSE) were used as the working, counter, and reference electrodes, respectively. The electrolyte was a 0.5 M Na_2SO_4 solution. The ac-impedance spectrum was measured with a 5 mV ac signal superimposed on the open circuit potential over the frequency range from 10^{-2} to 10^5 Hz. The cyclic voltammetry (CV) measurement was performed in the potential range of -0.4 to 0.4 V (vs. SMSE) with a scan rate in the range of 2–200 mV s^{-1}.

According to the CV curve, the specific capacitance of the electrode active material can be calculated as

$$C_{SC} = \frac{1}{v\Delta V} \int_{V_1}^{V_2} I(V)\mathrm{d}V \, , \tag{1}$$

where C_{SC} is the specific capacitance, $\Delta V = V_2 - V_1$ is the voltage range, v is the scan rate, and $I(V)$ is the current density based on the weight of the electrode active material.

The galvanostatic charge–discharge behavior of the electrodes was measured in the voltage window of -0.4 to 0.4 V. According to the obtained charge–discharge curves, the specific capacitance can also be calculated as

$$C_{SC} = \frac{I\Delta t}{m\Delta E}, \tag{2}$$

where I is the charge–discharge current, Δt is the discharge time, m is the weight of the electrode active material, and ΔE is the width of the voltage window.

3 Results and discussion

Figure 1a–c shows the general morphology and detailed microstructure of a typical α-MnO$_2$@CPF slab prepared by 1-min deposition in an aqueous solution containing 2 M H$_2$SO$_4$ and 0.5 M MnSO$_4$. It can be observed that under the deposition condition, a uniform MnO$_2$ coating is obtained on the entire carbon fiber surfaces (Fig. 1a and b). In addition, the electrodeposited MnO$_2$ particles show a nanosphere-shaped architecture with a dimension of several nanometres and hundreds of nanospheres forming many small pores (Fig. 1c). When the deposition time increases to 2 min (Fig. 1d–f), the morphology characteristics are much more obvious. This is different from the nanoflower or nanowhisker morphology of MnO$_2$ deposited from conventional neutral MnSO$_4$ solutions (shown as SD Fig. S1) [19, 21, 26].

Figure 2a shows the XRD patterns of MnO$_2$ deposited from the acidic MnSO$_4$ solution. Although the peaks are broad and weak due to the small particle size and poor crystallinity of the deposit, they all can be assigned to the cryptomelane-type MnO$_2$ (JCPDS 42-1348) with structural tunnels of 2×2 [MnO$_6$]. To further investigate the microstructure of the MnO$_2$, high-resolution TEM (HR-TEM) analysis was carried out on the MnO$_2$ deposited from the acidic MnSO$_4$

solution and the HR-TEM image is presented in Fig. 2b. It reveals a random crystal orientation of the α-MnO$_2$ particles. According to the fast Fourier transform (FFT) pattern in the inset of Fig. 2b, the interplanar spacing between the adjacent lattice planes is approximately 0.69 nm, corresponding to the (110) crystal plane of α-MnO$_2$. For comparison, ε-MnO$_2$ deposited from a neutral MnSO$_4$ solution containing 0.5 M Na$_2$SO$_4$ and 0.5 M MnSO$_4$ was also analyzed and the XRD patterns are presented in Fig. 2. Obviously, the deposit obtained from the neutral solution shows a akhtenskite-type structure (ε-MnO$_2$) (JCPDS 89-5171), a similar structure of γ-MnO$_2$ but with higher disorder [27].

The manganese valences and chemical composition of the two types of MnO$_2$ were estimated by XPS. Based on the multiplet splitting of the Mn 3s core-level spectra in Fig. 3a, b, the average manganese oxidation states are estimated to be about $+3.8$ for both of the MnO$_2$. The O1s spectra in Fig. 3c, d imply that both the oxides may exist as the form of MnO$_x$(OH)$_y \cdot z$H$_2$O. The electrode process of MnO$_2$ formation can be described as Eqs (3)–(10), among which Eqs (6)–(10) are believed to be the rate-determination steps [28]. These results suggest that high concentration of H$^+$ in the MnSO$_4$ solution not only slows the formation process of MnO$_2$ down but also promote the intermediate species to assemble into the cryptomelane-type structure with 2×2 [MnO$_6$] tunnels. Compared with the ε-type manganese oxide, the α-type oxide has a more positive free energy of formation [29], and thus tends to form spherical particles so as to reduce the surface area and free energy of itself.
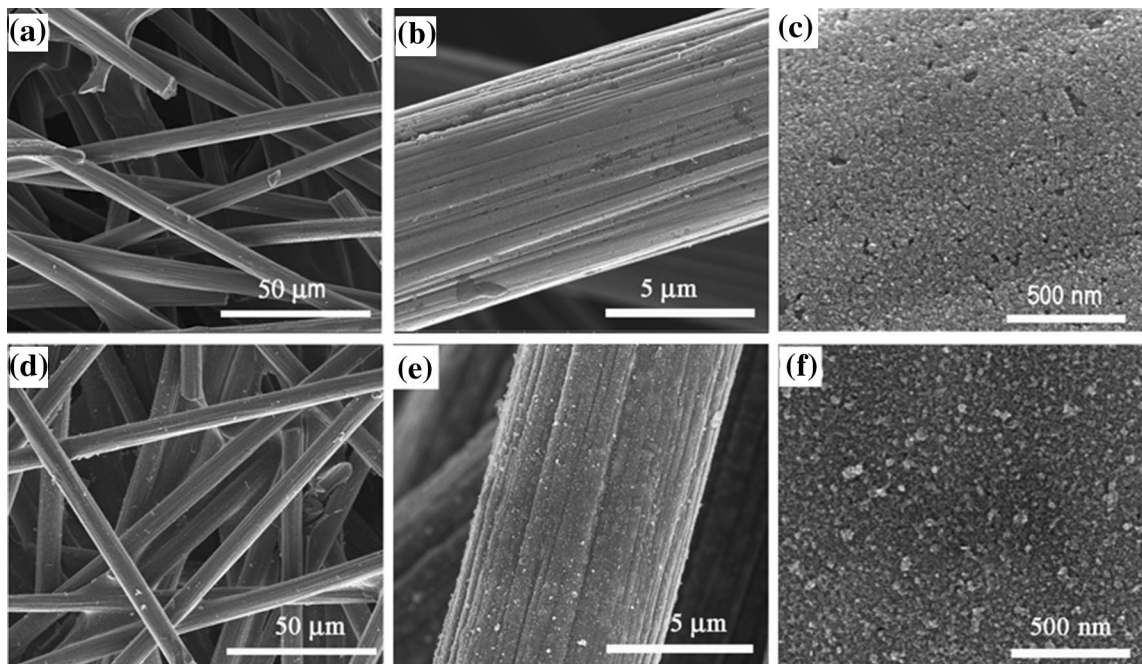

Fig. 1 FESEM images of the α-MnO$_2$@CFP after 1-min (**a**–**c**) and 2-min (**d**–**f**) deposition in the acidic MnSO$_4$ solution
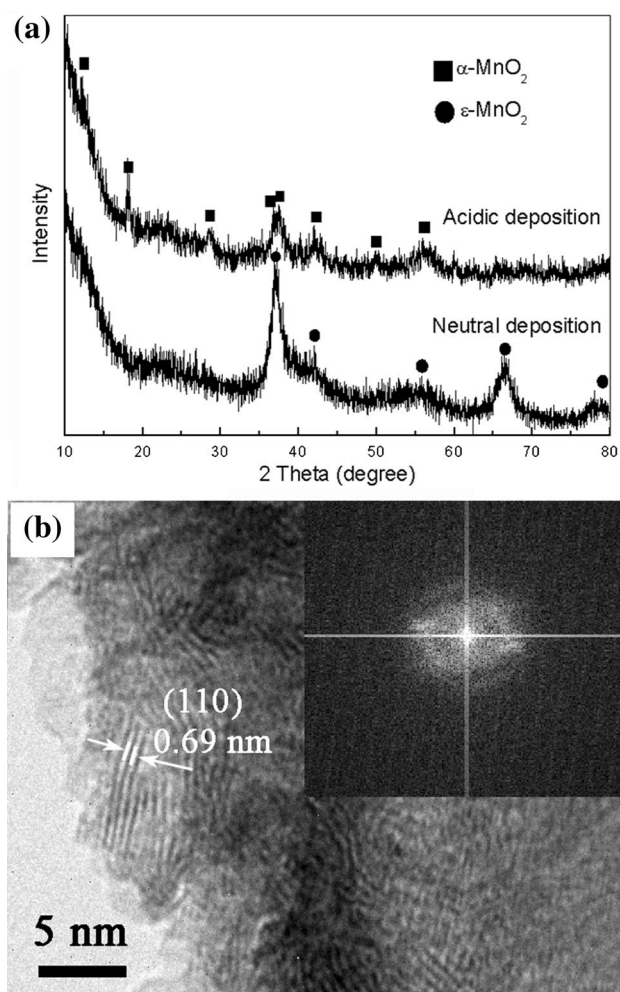
Fig. 2 **a** XRD patterns of the α-MnO$_2$ and ε-MnO$_2$ and **b** HR-TEM image of the α-MnO$_2$

$$[Mn(H_2O)_n]^{2+} \rightarrow [Mn(H_2O)_n]^{3+} + e \quad (3)$$

$$2[Mn(H_2O)_n]^{3+} \rightarrow [Mn(H_2O)_n]^{2+} + [Mn(H_2O)_n]^{4+} \quad (4)$$

$$[Mn(H_2O)_n]^{2+} \rightarrow [Mn(H_2O)_n]^{4+}_{ad} + 2e \quad (5)$$
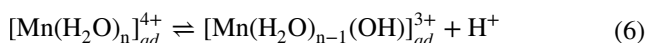
$$[Mn(H_2O)_n]^{4+}_{ad} \rightleftharpoons [Mn(H_2O)_{n-1}(OH)]^{3+}_{ad} + H^+ \quad (6)$$

$$[Mn(H_2O)_{n-1}(OH)]^{3+}_{ad} \rightleftharpoons [Mn(H_2O)_{n-2}(OH)_2]^{2+}_{ad} + H^+ \quad (7)$$

$$[Mn(H_2O)_{n-2}(OH)_2]^{2+}_{ad} \rightleftharpoons [Mn(H_2O)_{n-3}(OH)_3]^{+}_{ad} + H^+ \quad (8)$$

$$[Mn(H_2O)_{n-3}(OH)_3]^{+}_{ad} \rightleftharpoons [Mn(H_2O)_{n-4}(OH)_4]_{ad} + H^+ \quad (9)$$

$$[Mn(H_2O)_{n-4}(OH)_4]_{ad} \rightleftharpoons MnO_x(OH)_{4-2x} \cdot mH_2O + (n + x - m - 4)H_2O \quad (10)$$
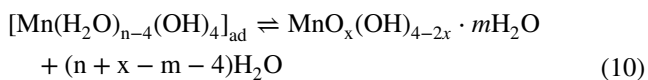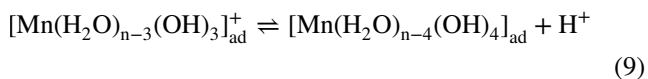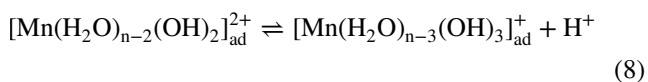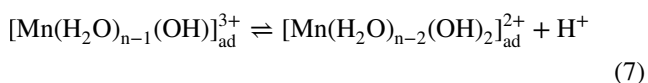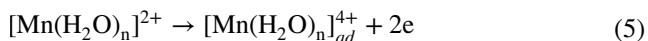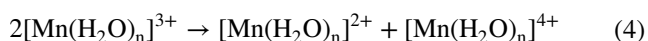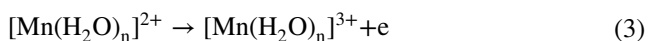
During the electrodeposition, it was found that the deposition current efficiency in the acidic solution was just about half of that in the neutral solution, and when deposition was carried out in the acidic solution, a red solution was clearly observed flowing out of the electrode slowly. This can be attributed to the fact that the $[Mn(H_2O)_n]^{3+}$ and $[Mn(H_2O)_n]^{4+}$ produced according to Eqs. (3) and (5) are much more stable in an acidic solution with a high H^+ concentration than in a neutral solution, and thus part of the ions can enter the solution by diffusion and migration.

For comparison of the electrochemical performance between the two types of MnO$_2$, α-MnO$_2$@CFP and ε-MnO$_2$@CFP electrodes were prepared from the acidic and neutral solutions, respectively. Considering the lower deposition current efficiency in the acidic solution, the deposition time in the acid solution was longer than that in the neutral solution so as to ensure that the electrodes have the same mass loading of MnO$_2$.

Figure 4a and b shows the rate-dependent CVs of the α-MnO$_2$@CFP and ε-MnO$_2$@CFP electrodes obtained by 1-min deposition in the acidic solution and 0.5-min deposition in the neutral solution, respectively. It can be seen that although the two electrodes have almost the same mass loading (0.11 and 0.12 mg cm^{-2}), the CV curve of the α-MnO$_2$@CFP shows higher current response than that of ε-MnO$_2$@CFP at the same scan rate. The specific capacitances (based on the active mass of MnO$_2$) for the α-MnO$_2$@CFP and ε-MnO$_2$@CFP electrodes are determined to be 422.3 and 329.4 F g^{-1} at 2 mV s^{-1}, respectively. As the scan rate increases, the current response increases and the CV curve for the ε-MnO$_2$@CFP electrode shows some distortions from an ideal capacitor, which is attributed to increasing over-potentials from ion transport between the electrolyte and MnO$_2$ [19]. However, the shape of CV curve for the α-MnO$_2$@CFP electrode remains rectangular. Further analyses of the curves show that when the scan rate increases from 2 to 100 and 200 mV s^{-1}, the capacitance losses for the α-MnO$_2$@CFP electrode are only 23 and 29%, respectively. But the corresponding losses for the ε-MnO$_2$@CFP electrode reach up to 35 and 44%, respectively. Since the α-MnO$_2$ and ε-MnO$_2$ are both deposited on the same CFP in the present work, the difference of capacitive performance between the corresponding electrodes must derive from the MnO$_2$. The α-MnO$_2$@CFP electrode also shows a better rate capability compared to the MnO$_2$@CNT or MnO$_2$@graphene electrodes prepared by deposition from neutral solutions as shown in Table 1 [21, 30].

Considering the fact that the CFP slab has a double-layer capacitance which may influence the determination of the capacitance value of MnO$_2$, CV tests were also carried out on a bare CPF electrode with a working area of 1 cm^2. Figure 4c shows the CV curves of the CFP and α-MnO$_2$@CFP electrodes at a scan rate of 2 mV s^{-1}. Compared to the
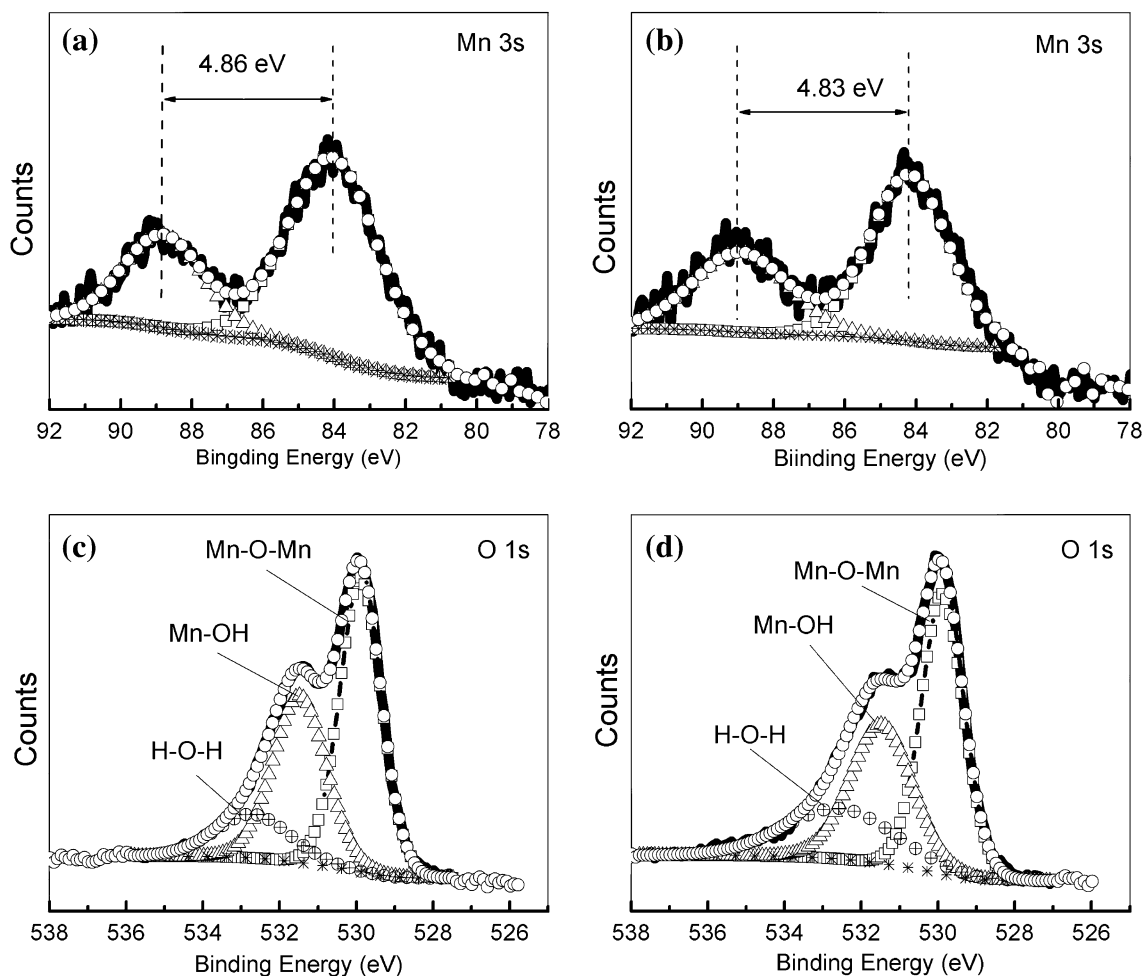
Fig. 3 Narrow-scan Mn 3s XPS spectra of the **a** α-MnO$_2$ and **b** ε-MnO$_2$; Narrow-scan O 1s XPS spectra of the **a** α-MnO$_2$ and **b** ε-MnO$_2$

α-MnO$_2$@CFP electrode, the CPF slab exhibits a lower current response. The specific capacitance of CPF slab is just about 9.2 mF g^{-1} (0.069 mF cm^2), which is much lower than that of α-MnO$_2$@CFP electrodes (46.5 mF cm^2). As a result, it could be concluded that the capacitance of CFP could be negligible for the composite electrodes.

Figure 4d summarizes the specific capacitances versus scan rates for the electrodes deposited for different times (the related CVs are presented in SD Fig. S2). As the deposition time increases, the specific capacitances of both types of electrodes decrease. This can be attributed to the fact that the pseudocapacitance is mainly derived from the electrochemical reaction (or absorption) in the surface layer of the electrode material [31]. The long deposition time leads to a thick inactive layer (deep layer) and thus reduces the total specific capacitance of the electrode material. The α-MnO$_2$@CFP electrodes obtained by 0.5-min deposition from the acidic solution (mass loading of MnO$_2$: 0.04 mg cm^{-2}) shows the highest capacitance and

best rate capability, the capacitance reaches to 623.9 F g^{-1} at 2 mV s^{-1}, and the capacitance losses are only 21 and 25% at 100 and 200 mV s^{-1}, respectively. When the deposition time increases to 2 min (the mass loading of MnO$_2$ increases to 0.30 mg cm^{-2}), the capacitance decreases to 326.7 F g^{-1} at 2 mV s^{-1}, and the capacitance loss is 37% at 200 mV s^{-1}. It is noted that although the ε-MnO$_2$@ CFP electrode prepared by 1-min deposition from the neutral solution has almost the same mass loading of MnO$_2$ (0.29 mg cm^{-2}) as the α-MnO$_2$@CFP electrode obtained by 2-min deposition from the acidic solution, it exhibits a capacitance of 238.2 F g^{-1} at 2 mV s^{-1}, and the capacitance loss reaches to about 56% at 200 mV s^{-1}. The α-MnO$_2$@CFP electrode also shows a better rate capability than the ε-MnO$_2$@CFP one. When the deposition time further increases to 3 min (mass loading of MnO$_2$: 0.49 mg cm^{-2}), the specific capacitance of the α-MnO$_2$@CFP electrode decreases to 271.7 F g^{-1} at 2 mV s^{-1}, and the capacitances losses are 31 and 43% at 100 and 200 mV s^{-1},
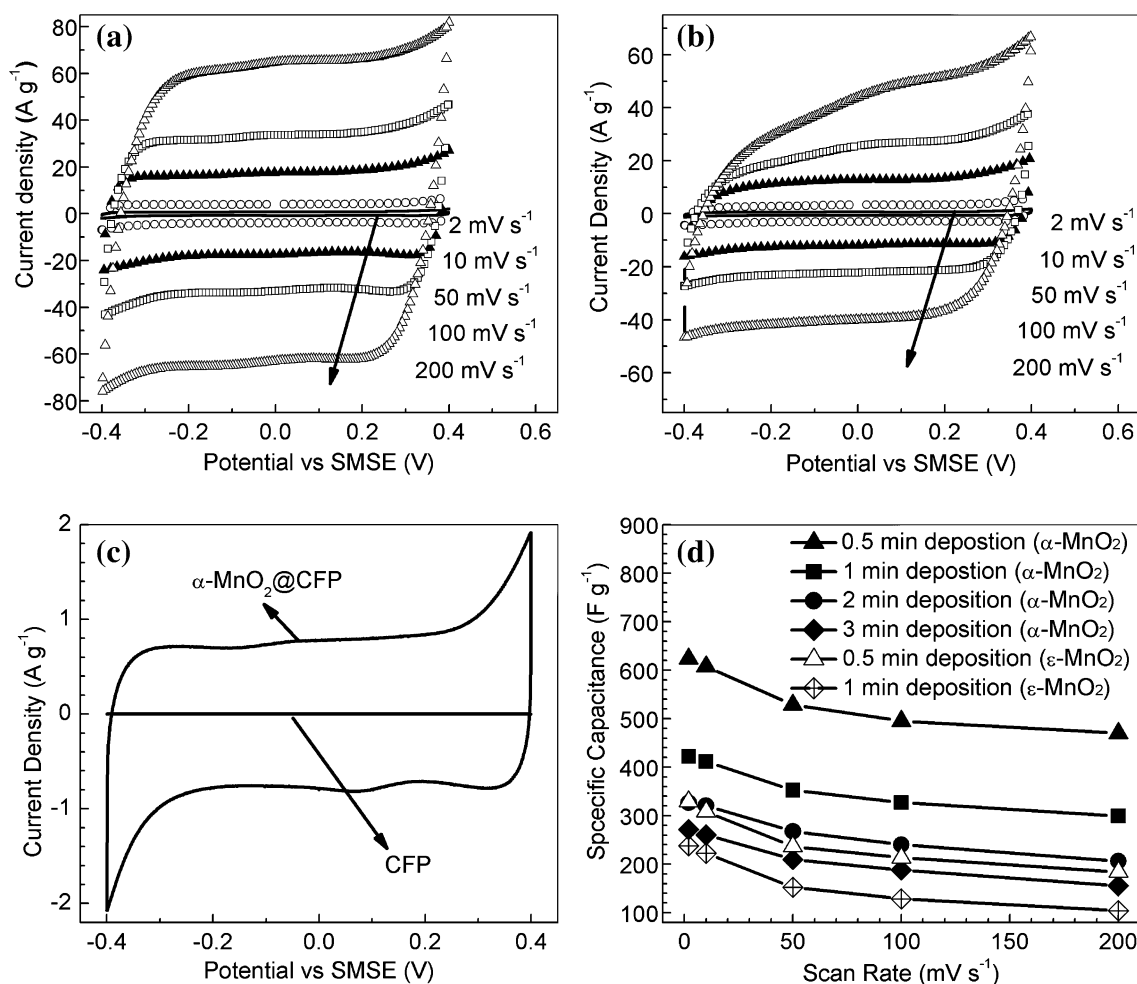
Fig. 4 Cyclic voltammograms of **a** the α-MnO$_2$@CPF electrode prepared by 1-min deposition from the acidic MnSO$_4$ solution and **b** the ε-MnO$_2$@CPF electrode prepared by 0.5-min deposition from the neutral MnSO$_4$ solution; **c** the α-MnO$_2$@CPF and a bare CPF electrodes at 2 mV s^{-1}; **d** Specific capacitances versus scan rates for the electrodes deposited for different times

Table 1 Capacitance and capacitance loss values estimated according to the capacitances versus scan rates data reported in the references

Substrate	Loading mass of MnO$_2$ /mg	Capacitance (2 mV s^{-1})/F g^{-1}	Capacitance loss (100 mV s^{-1}) (%)	Capacitance loss (200 mV s^{-1})	References
CNTs@sponge	0.04	590	33	–	[21]
CNTs@sponge	0.1	440	33	–	[21]
Graphene foam	0.1	465	53	62%	[30]
Au@WO$_3$ nano wire@carbon fiber	0.14	588 (10 mV s^{-1})	63	–	[32]
Graphene@textile	0.3	315	65	–	[19]
Graphene foam	0.42	290	69	79%	[30]
CNTs@ sponge	0.5	195	59	–	[21]

respectively. The rate capability of the α-MnO$_2$@CPF electrode is still much better than those of the electrodes with almost the same mass loading of MnO$_2$ reported in the literature [21, 30]. From the data obtained in this work and reported in the literatures (as shown in Table 1) [19, 21, 30, 32], it can be found that the substrate or current collector with a high specific surface area and conductivity can greatly improve the capacitance of MnO$_2$ at a low scan rate but seems to have little impact on the rate capability of the active material. On the other hand, the [MnO$_6$]

tunnel structure of MnO_2 plays an important role in both the capacitance and rate capability of the material.

Galvanostatic charge–discharge tests were also performed with different current densities in a stable voltage window of −0.4 to 0.4 V, as shown in Fig. 5a. The linear voltage–time profiles and the nearly symmetric charge–discharge characteristics indicate good capacitive behavior with a rapid I~V response for these electrodes. When the charge–discharge current density increases from 0.5 to 10 A g^{-1}, the capacitance for the α-MnO_2@CFP electrode decreases from 431.9 to 346.2 F g^{-1}. The capacitance retention of the electrode is about 80%, whereas the retention for the ε-MnO_2@CFP electrode is just 66% at the same current densities. This is consistent with the CV results. In addition, the α-MnO_2@CFP electrode shows an acceptable cycling stability performance at the current density of 1 A g^{-1} (Fig. 5b). The capacitance decreases from 412.1 to 384.7 F g^{-1} after 100 cycles, and then decreases slowly to 375.2 F g^{-1} after 3500 cycles.

Figure 5c presents the impedance spectra of the electrodes measured at the initial open circuit potentials (OCPs). It can be seen that each of the measured impedance spectra consists of a depressed arc at high frequencies (shown in the inset), a straight line inclined at a constant phase angle to the real axis (Warburg region) at intermediate frequencies and a vertical capacitive line at low frequencies. It is generally demonstrated that the diameter of the arc reflects the charge-transfer resistance related to the electrochemical reaction at the electrode/electrolyte interface. With an equivalent circuit model (shown as SD Fig. 3S; Table 1S), the impedance spectra can be fitted well and the results show that the α-MnO_2@CFP electrode has much lower charge-transfer and diffusion resistances than the ε-MnO_2@CFP one. The diffusion resistances (W1-R) for the α-MnO_2@CFP and ε-MnO_2@CFP are about 1.0 and 12.8 Ω $s^{-1/2}$, respectively. These results indicate that the 2×2 [MnO_6] tunnels in the α-MnO_2 (shown in Fig. 5d) offer facile diffusion paths for cations and thus make more reactive sites available in the inner-surface layer

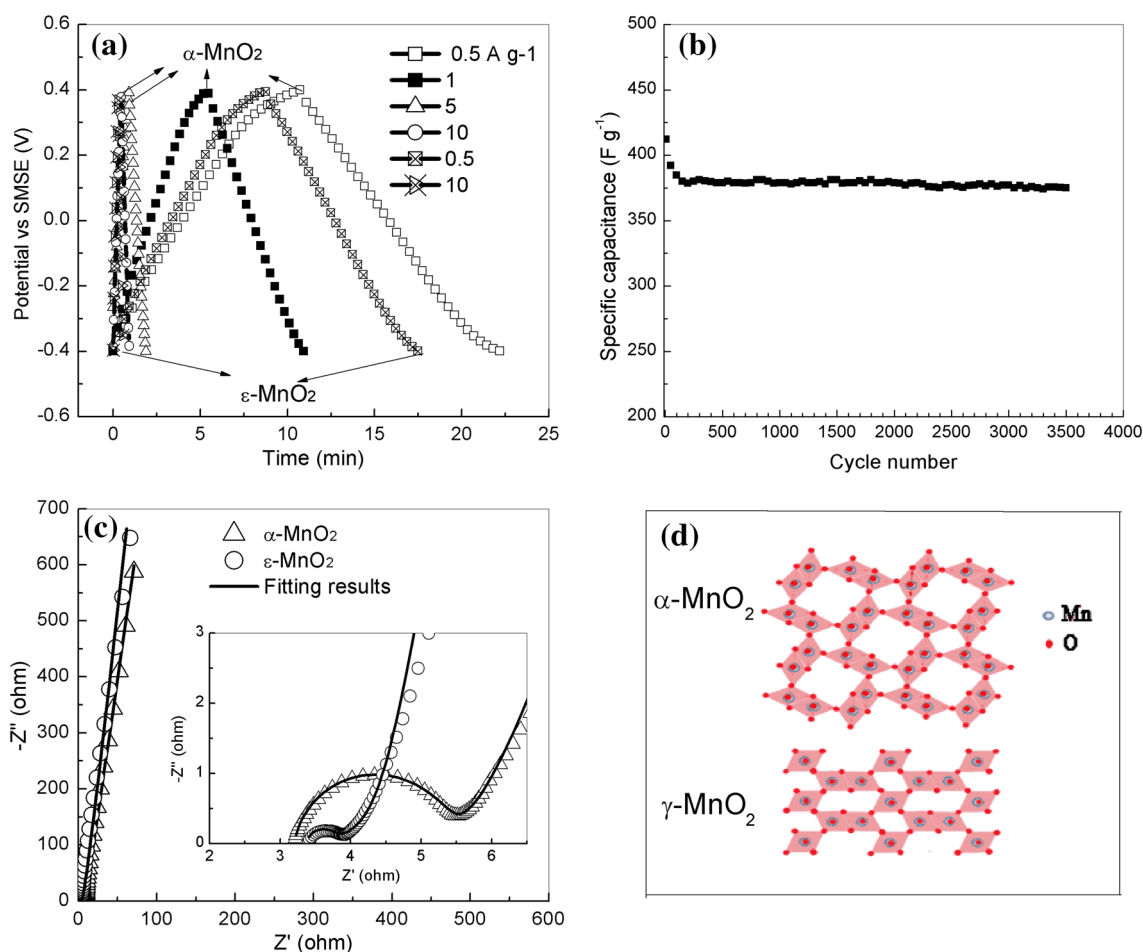**Fig. 5** **a** Galvanostatic charge–discharge curves of the α-MnO_2@CFP and ε-MnO_2@CFP electrodes; **b** Cycle performance of the α-MnO_2@CFP electrode at 1 A g^{-1}; **c** Impedance spectra of the α-MnO_2@CFP and ε-MnO_2@CFP electrodes, the high frequency part of the impedance spectra (inset); **d** Crystal structures of MnO_2

of the active material [22, 32]. Obviously, the facile diffusion paths and plentiful reactive sites can accelerate the kinetics of the inner-surface redox reactions associated with the energy storage process and thus lead to symmetrical CV curves and high rate capability. In addition, the suitable diffusion tunnels may extend the insertion depth of cations, which increase the utilization and specific capacitance of the active material.

4 Conclusions

A simple electrochemical method was used to produce α-MnO$_2$ on carbon fibers and the obtained oxide was evaluated as the active materials for binder-free electrodes of supercapacitors. The obtained α-MnO$_2$@CFP electrode exhibits a higher capacitance and better rate capability compared to the ε-MnO$_2$@CFP electrode prepared by the conventional electrochemical method. For the α-MnO$_2$@CFP electrode, a specific capacitance of 623.9 F g^{-1} can be achieved at 2 mV s^{-1} and the capacitance retention is up to 75% at 200 mV s^{-1}. The rate capability is also the best for most of the binder-free MnO$_2$/carbon electrodes reported in previous studies. These superiorities mainly result from the specific tunnel structure of α-MnO$_2$ which offers not only facile diffusion paths for cations but also plentiful reactive sites for the inner-surface redox reactions associated with the energy storage process. Although the present research has focused on growth of MnO$_2$ on CFP for supercapacitors, it can be expected that better electrochemical performance could be achieved when a carbon support with much higher specific area, such as CNTs and graphene, is used as the carbon backbone. In summary, this facile electrochemical approach can offer great promise in the development of high-performance binder-free MnO$_2$ electrodes for energy storage devices.

References

1. Simon P, Gogotsi Y (2008) Materials for electrochemical capacitors. Nat Mater 7:845–854
2. Chmiola J, Yushin G, Gogotsi Y, Portet C, Simon P, Taberna PL (2006) Anomalous increase in carbon capacitance at pore sizes less than 1 nanometer. Science 313:1760–1763
3. Hall PJ, Mirzaeian M, Fletcher SI, Sillars FB, Rennie AJR, Shitta-Bey GO, Wilson G, Cruden A, Carter R (2010) Energy storage in electrochemical capacitors: designing functional materials to improve performance. Energy Environ Sci 3:1238–1251
4. Xu CJ, Kang FY, Li BH, Du HD (2010) Recent progress on manganese dioxide based supercapacitors. J Mater Res 25:1421–1432
5. Wei WF, Cui XW, Chen WX, Ivey DG (2011) Manganese oxide-based materials as electrochemical supercapacitor electrodes. Chem Soc Rev 40:1697–1721
6. Fan Z, Yan J, Wei T, Zhi L, Ning G, Li T (2011) Asymmetric supercapacitors based on graphene/MnO$_2$ and activated carbon nanofiber electrodes with high power and energy density. Adv Funct Mater 21:2366–2375
7. Kazemi SH, Kianic MA, Ghaemmaghami M, Kazemi H (2016) Nano-architectured MnO$_2$ electrodeposited on the Cu-decorated nickel foam substrate as supercapacitor electrode with excellent areal capacitance. Electrochim Acta 197:107–116
8. Akbulut S, Yilmaz M, Raina S, Hsu S-H, Kang WP (2017) Advanced supercapacitor prototype using nanostructured double-sided MnO$_2$/CNT electrodes on flexible graphite foil. J Appl Electrochem 47:1035–1044
9. Majumdar D, Bhattacharya SK (2017) Sonochemically synthesized hydroxy-functionalized graphene–MnO$_2$ nanocomposite for supercapacitor applications. J Appl Electrochem 47:789–801
10. Zhang SW, Peng C, Ng KC, Chen GZ (2010) Nanocomposites of manganese oxides and carbon nanotubes for aqueous supercapacitor stacks. Electrochim Acta 55:7447–7453
11. Gong LY, Su LH, Jiang HY (2011) Rapid synthesis of homogeneous MnO$_2$/multi-wall carbon nanotubes nanostructure and its electrochemical capacitive behavior. Mater Lett 65:1588–1590
12. Wang J-W, Chen Y, Chen B-Z (2016) Synthesis and control of high-performance MnO$_2$/carbon nanotubes nanocomposites for supercapacitors. J Alloy Compd 688:184–197
13. Sharma RK, Oh H-S, Shul Y-G, Kim H (2007) Carbon-supported, nano-structured, manganese oxide composite electrode for electrochemical supercapacitor. J Power Sources 173:1024–1028
14. Kim M, Hwang Y, Min K, Kim J (2013) Introduction of MnO$_2$ nanoneedles to activated carbon to fabricate high-performance electrodes as electrochemical supercapacitor. Electrochim Acta 113:322–331
15. Zhang YF, Zhang CX, Huang GX, Xing BL, Duan YL (2015) Synthesis and capacitive properties of manganese oxide nanoparticles dispersed on hierarchical porous carbons. Electrochim Acta 166:107–116
16. Liu Z, Tan XL, Gao X, Song LH (2014) Synthesis of three-dimensionally ordered macroporous manganese dioxide–carbon nanocomposites for supercapacitors. J Power Sources 267:812–820
17. Lei Y, Fournier C, Pascal JL, Favier F (2008) Mesoporous carbon–manganese oxide composite as negative electrode material for supercapacitors. Microporous Mesoporous Mater 110:167–176
18. Liu Y, Yan D, Li YH, Wu ZG, Zhuo RF, Li SK, Feng JJ, Wang J, Yan PX, Geng ZR (2014) Manganese dioxide nanosheet arrays grown on graphene oxide as an advanced electrode material for supercapacitors. Electrochim Acta 117:528–533
19. Yu GH, Hu LB, Vosgueritchian M, Wang HL, Xie X, McDonough JR, Cui X, Cui Y (2011) Solution-processed graphene/MnO$_2$ nanostructured textiles for high-performance electrochemical capacitors. Nano Lett 11:2905–2911
20. Kim JH, Lee KH, Overzet LJ, Lee GS (2011) Synthesis and electrochemical properties of spin-capable carbon nanotube sheet/MnO$_x$ composites for high-performance energy storage devices. Nano Lett 11:2611–2617
21. Chen W, Rakhi RB, Hu LB, Xie X, Cui Y, Alshareef HN (2011) High-performance nanostructured supercapacitors on a sponge. Nano Lett 11:5165–5172
22. Donne SW, Feddrix FH, Glöckner R, Marion S, Norby T (2002) Water and protons in electrodeposited MnO$_2$ (EMD). Solid State Ionics 152–153:695–701

23. Aziz RA, Jose R (2017) Charge storage capability of tunnel MnO_2 and alkaline layered $Na-MnO_2$ as anode material for aqueous asymmetry supercapacitor. J Electroanal Chem 799:538–546

24. Chen S, Zhu JW, Wu XD, Han QF, Wang X (2010) Graphene oxide MnO_2 nanocomposites for supercapacitors. ACS Nano 4:2822–2830

25. Poyraz AS, Huang J-P, Pelliccione CJ, Tong X, Cheng S-B, Wu LJ, Zhu YM, Marschilok AC, Takeuchi KJ, Takeuchi ES (2017) Synthesis of cryptomelane type α-MnO_2 ($K_xMn_8O_{16}$) cathode materials with tunable K^+ content: the role of tunnel cation concentration on electrochemistry. J Mater Chem A 5:16914–16928

26. Sun LM, Wang XH, Zhang K, Zou JP, Zhang Q (2016) Metal-free $SWNT/carbon/MnO_2$ hybrid electrode for high performance coplanar micro-supercapacitors. Nano Energy 22:11–18

27. Nawaz F, Cao HB, Xie YB, Xiao JD, Chen Y, Ghazi ZA (2017) Selection of active phase of MnO_2 for catalytic ozonation of 4-nitrophenol. Chemosphere 168:1457–1466

28. Tan ZZ, Mei GG, Li WJ, Zeng KX (2004) Metallurgy of manganese, Central South University Press, Changsha

29. Kitchaev DA, Dacek ST, Sun W, Ceder G (2017) Thermodynamics of phase selection in MnO_2 framework structures through alkali intercalation and hydration. J Am Chem Soc 139:2672–2681

30. He YM, Chen WJ, Li XD, Zhang ZX, Fu JC, Zhao CH, Xie EQ (2013) Freestanding three-dimensional graphene/MnO_2 composite networks as ultralight and flexible supercapacitor electrodes. ACS Nano 7:147–182

31. Conway BE (1999) Electrochemical supercapacitors: scientific fundamentals and technological applications. Kluwer/Plenum, New York

32. Lu XH, Zhai T, Zhang XH, Shen YQ, Yuan LY, Hu B, Gong L, Chen J, Gao YH, Zhou J, Tong YX, Wang ZL (2012) $WO_{3-x}@Au@MnO_2$ core–shell nanowires on carbon fabric for high-performance flexible supercapacitors. Adv Mater 24:938–944